the wave function at $(x+2\pi/hb,y)$ with its value at (x,y), the magnitude is the same but the phase is changed by $2\pi q_x/hb$, because of the phase-factor $e^{iq_x x}$ in (54a). There is no such periodicity over a distance $2\pi/ha$ in the y direction because the wave-function amplitudes are not periodic in the network in Fig. 6 since the phase shifts at A_l and A_l' depend on l according to (36). This is what we would expect by setting up the wave function as a Pippard network[8] in the Landau gauge used in this paper.

8. CONCLUDING REMARKS

We have set up the theory of the effective Hamiltonian in terms of Wannier functions and difference equations. This method can be used to derive the wave functions in configuration space, and it is hoped that this approach gives a clear picture of the situation as well as of the problems involved. It is certainly one of the more elementary methods, since all the matrix elements are finite and do not involve δ functions. When breakdown is liable to occur, the Wannier functions have to be modified, and than the effective Hamiltonian must be treated, at least in the regions of breakdown, as a matrix.

The use of such a theory has enabled us to justify the network model used by the author,[10] which can readily be shown to be essentially equivalent to those used by Pippard.[7,8] Then we have considered the problem of the de Haas–van Alphen effect with breakdown. The results are very much as we might expect. Finally, we have shown how to construct a wave function lying on a network as suggested by Pippard.[7,8]

All this has been done in the framework of a simple rectangular model. For the sake of completeness the theory should be extended to deal with more complicated models, but the author does not expect that any surprising new results would be found. The problem of spin-orbit coupling has not been treated and it may be important, particularly when the band gaps across which breakdown takes place are produced primarily by spin-orbit coupling. In this case we would have to consider the effect of the first-order term in the effective Hamiltonian expanded as a power series in h.

ACKNOWLEDGMENTS

The author would like to thank Professor E. Brown, Professor L. M. Falicov, and Professor G. Trammell for their help in discussing some of the topics in this article.

PHYSICAL REVIEW VOLUME 149, NUMBER 2 16 SEPTEMBER 1966

Band Structure and Fermi Surface of White Tin*†

GIDEON WEISZ‡

Department of Physics and Institute for the Study of Metals, University of Chicago, Chicago, Illinois

(Received 4 February 1966)

The band structure and Fermi surface of metallic white tin are successfully calculated, using a local-pseudopotential approximation. A new, simple, and accurate model is found for including the spin-orbit coupling within the framework of a pseudopotential Hamiltonian. The results are compared with experimental data, and good agreement is found throughout.

I. INTRODUCTION

THIS paper contains a theoretical calculation of the band structure and Fermi surface of white tin, and a comparison of the results with experimental data. It also introduces a new method for dealing with the spin-orbit interaction. The study of tin is motivated by many circumstances and considerations. These are discussed in the following paragraphs, beginning with the experimental situation and proceeding to the problems and possibilities to which the tin lattice structure gives rise.

In recent years, the Fermi surface of tin metal has been the subject of a number of experimental investigations, but the complexity of the surface has thus far prevented it from being fully understood. The present calculation by a pseudopotential method is intended to furnish a guide and a stimulus to further experimentation. The following experiments have shed some light on the electronic structure of Sn: de Haas–van Alphen effect,[1] galvanomagnetic properties,[2–4] cyclotron size

* Supported in part by the National Science Foundation.

† Submitted in partial fulfillment of the requirements for the degree of Doctor of Philosophy at the University of Chicago, Chicago, Illinois.

‡ Present address: Division of Engineering and Applied Physics, Harvard University, Cambridge, Massachusetts.

[1] A. V. Gold and M. G. Priestley, Phil. Mag. **5**, 1089 (1960).

[2] N. E. Alekseevskii, Yu. P. Gaidukov, I. M. Lifshitz, and V. G. Peschanskii, Zh. Eksperim. i Teor. Fiz. **39**, 1201 (1960) [English transl.: Soviet Phys.—JETP **12**, 837 (1961)].

[3] N. E. Alekseevskii and Yu. P. Gaidukov, Zh. Eksperim. i Teor. Fiz. **41**, 1079 (1961) [English transl.: Soviet Phys.—JETP **14**, 770 (1962)].

[4] R. C. Young, Phys. Rev. Letters **15**, 262 (1965).

effects,[5–7] drift size effect,[8] ordinary[9] and special[10,11] cyclotron resonance, magnetoacoustic attenuation,[12–15] and anomalous skin effect.[16,17] The superconductivity experiments[18] should also be mentioned here. By virtue of its tetragonal crystal structure, tin exhibits a marked anisotropy in many of its properties. It is the most anisotropic of known superconducting elements. The calculation[19] of the anisotropy of the energy gap is thus of some interest, but it cannot be done without a detailed picture of the Fermi surface such as is furnished by the present calculation.

An attractive feature of tin is its obtainability at a very high purity. At liquid-helium temperatures, mean free paths of the order of a millimeter make possible or practical experiments such as Gantmakher's rich, almost pictorial, size-effect experiments.[6,7] Such effects will undoubtedly be studied in detail from a theoretical standpoint. It will then be useful to have available for comparison both Gantmakher's experiment and a picture of the Fermi surface which it measures. For example, the present calculation should give us some idea as to what kinds of Fermi surface correspond to each of the several line shapes that Gantmakher has encountered.

The success of local-pseudopotential calculations of the band structures and Fermi surfaces of numerous simple metals gives us confidence in applying this method to tin. In particular, we are encouraged by the especially relevant examples of Ge,[20] Sb,[21] and Pb,[22] which are neighbors of Sn in the periodic table. However, the Fermi surface is usually determined primarily by the values of the band energies near a few symmetry points. The complexity and extent of the pieces of Fermi surface in tin provide a somewhat more taxing test than is usual of the efficacy of the local pseudopotential approximation.

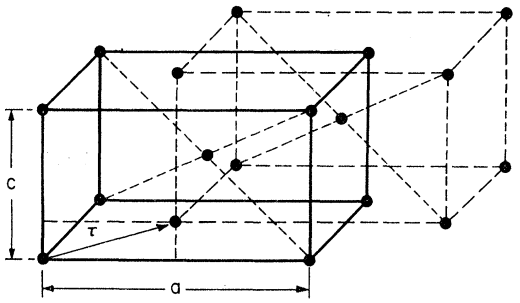

FIG. 1. The crystal lattice of white tin.

Tin has an atomic number 50, so that its electrons should experience a considerable spin-orbit interaction. The spin-orbit interaction is of great importance in heavy elements like lead, where it is about 1.7 eV for the $P_{3/2}$–$P_{1/2}$ splitting of Pb II. In tin it is considerably weaker, about 0.5 eV for the corresponding splitting, but its importance is greatly enhanced by the noncubic crystal structure. The A5 white-tin lattice has two atoms per unit cell, and its space-group properties result in sticking-together of the spinless bands in pairs along two symmetry lines on the Brillouin-zone faces.[23,24] The spin-orbit interaction lifts this degeneracy at all points but two. Thus the effects of spin are of essential importance in tin. They must be taken into account, if possible, not as a perturbation but on the same footing as the crystal pseudopotential. Tin thus provides an interesting opportunity to test a new, simple way of incorporating the spin-orbit interaction into a pseudopotential secular equation. This method is developed in Sec. III.

Finally, while tin is the only example of the A5 lattice structure at normal pressures and temperatures, germanium and silicon are known to take the more compact white-tin structure at higher pressures.[25] To investigate the high-pressure behavior of these materials, calculations such as the present one will be necessary. Many of the general features of the band structure of white tin may be expected to persist, and in that sense this calculation should serve as a model or starting point for the others.

Section II describes the white-tin lattice and its Brillouin zone, as well as the method of calculation and the resulting band structure. Section III develops the present formulation of the spin-orbit interaction, and describes the influence of spin upon the band structure. Section IV is devoted to a description of the resulting Fermi surface. Section V compares the results with the available experimental data. Section VI is a brief discussion of the results.

[5] M. S. Khaikin, Zh. Eksperim. i Teor. Fiz. **43**, 59 (1962) [English transl.: Soviet Phys.—JETP **16**, 42 (1963)].
[6] V. F. Gantmakher, Zh. Eksperim. i Teor. Fiz. **44**, 811 (1963) [English transl.: Soviet Phys.—JETP **17**, 549 (1963)].
[7] V. F. Gantmakher, Zh. Eksperim. i Teor. Fiz. **46**, 2028 (1964) [English transl.: Soviet Phys.—JETP **19**, 1366 (1964)].
[8] V. F. Gantmakher and E. A. Kaner, Zh. Eksperim. i Teor. Fiz. **45**, 1430 (1963) [English transl.: Soviet Phys.—JETP **18**, 988 (1964)].
[9] M. S. Khaikin, Zh. Eksperim. i Teor. Fiz. **42**, 27 (1962) [English transl.: Soviet Phys.—JETP **15**, 18 (1963)].
[10] J. F. Koch and A. F. Kip, Phys. Rev. Letters **8**, 473 (1962)
[11] M. S. Khaikin, Zh. Eksperim. i Teor. Fiz. **39**, 513 (1960) [English transl.: Soviet Phys.—JETP **12**, 359 (1961)].
[12] A. A. Galkin, E. A. Kaner, and A. P. Korolyuk, Zh. Eksperim. i Teor. Fiz. **39**, 1517 (1960) [English transl.: Soviet Phys.—JETP **12**, 1055 (1961)].
[13] T. Olsen, J. Phys. Chem. Solids, **24**, 649 (1963).
[14] B. I. Miller (to be published).
[15] R. J. Kearney, A. R. Mackintosh, and R. C. Young, Phys. Rev. **140**, A1671 (1965).
[16] E. Fawcett, Proc. Roy. Soc. (London) **A232**, 519 (1955).
[17] R. G. Chambers, Can. J. Phys. **34**, 1395 (1956).
[18] D. H. Douglass, Jr., and L. M. Falicov, *Progress in Low Temperature Physics*, edited by C. J. Gorter (North-Holland Publishing Company, Amsterdam, 1964).
[19] A. Bennett, Phys. Rev. **140**, 1902 (1965).
[20] D. Burst, Phys. Rev. **134**, A1337 (1964).
[21] L. M. Falicov and P. J. Lin, Phys. Rev. **141**, 562 (1966).
[22] R. Anderson and A. Gold, Phys. Rev. **139**, 1459 (1965).
[23] S. Mase, J. Phys. Soc. Japan **14**, 1538 (1959).
[24] M. Miasek and M. Suffczynski, Bull. Acad. Polon. Sci. Ser. Sci. Math. Astron. Phys. **9**, 483 (1961).
[25] T. Yoshioka and P. A. Beck, Trans. Met. Soc. AIME **233**, 1788 (1965).

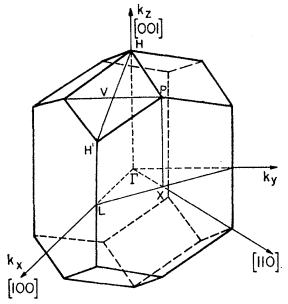

FIG. 2. The Brillouin zone.

II. CALCULATION OF THE BAND STRUCTURE

A. Crystal Structure

The white-tin structure is shown in Fig. 1. It may be viewed as a body-centered tetragonal lattice with two atoms per unit cell. The lattice constants, extrapolated to 0°K,[26] are

$$a=5.80\ \text{Å},$$
$$c=3.15\ \text{Å}.$$

The ratio

$$\mu=a/c=1.84$$

shows that the lattice is far from being cubic. The primitive vectors of the direct and reciprocal lattices are given in Tables I and II, respectively. The Brillouin zone is shown in Fig. 2. The coordinates of the symmetry points are listed in Table II. Throughout this paper, energies will be quoted in rydbergs, and k vectors in units of $k_0=2\pi/a=1.08\times10^8$ cm^{-1}.

B. The Pseudopotential

A pseudopotential model is used in this calculation, and the pseudopotential coefficients required are determined by fitting them to a few well selected experimental data. The pseudopotential approach is by now established as a convenient and flexible framework for the study of many problems, among them the electronic structure of simple metals, semimetals, and semiconductors. The following paragraphs contain a brief exposition and interpretation of the pseudopotential formalism as we use it here.

Suppose that $|\psi_v\rangle$ is the wave function of a valence electron, so that the spinless crystal Schrödinger equation is given by

$$\mathcal{H}_0|\psi_v\rangle=((1/2m)p^2+V)|\psi_v\rangle=E|\psi_v\rangle. \quad (2.1)$$

Let $\mathcal{P}_c$ be the operator which projects any function onto the space $\mathcal{S}^c$ spanned by the core orbitals $|b_t\rangle$, and let $\mathcal{P}_v$ be the corresponding projection operator for the space $\mathcal{S}^v$ of the valence solutions. Thus,

$$\mathcal{P}_c=\sum_t |b_t\rangle\langle b_t| \quad (2.2)$$

and

$$\mathcal{P}_v+\mathcal{P}_c=1, \quad \text{or} \quad \mathcal{P}_v=1-\mathcal{P}_c. \quad (2.3)$$

These projection operators commute with the Hamiltonian, i.e., they satisfy the useful relations

$$\mathcal{P}\mathcal{H}_0=\mathcal{H}_0\mathcal{P}, \quad (2.4)$$
$$\mathcal{P}^2=\mathcal{P}.$$

Now $|\psi_v\rangle$ satisfies the equation

$$[\mathcal{P}_v\mathcal{H}_0\mathcal{P}_v]|\psi_v\rangle=\mathcal{H}_0'|\psi_v\rangle=E|\psi_v\rangle. \quad (2.5)$$

The new operator $\mathcal{H}_0'$ is in a very important respect superior to its parent when $|\psi_v\rangle$ is expressed in terms of a finite basis. Its advantage is that it effectively removes from the problem an undesirable subspace, which contains no part of the solution. This supplementary condition is quite important here, for the following reason. A small set of plane waves adequately represents the valence wave functions outside the relatively small core regions. But the core wave functions have an entirely different character, being essentially similar to bound states. That is, they are concentrated in a small region, so that their Fourier or plane-wave expansions are of not negligible size in a rather extended region in k space. Thus, it would take a very large number of plane waves to remove effectively the undesirable subspace, and thus its influence, from the problem. The term "undesirable" is used here with a serious intent, as the corresponding error ΔE_{err} in the energy of an approximate valence wave function $|\phi\rangle$ is

$$\Delta E_{\text{err}}=\langle\phi|\mathcal{P}_c(E-\mathcal{H}_0)\mathcal{P}_c|\phi\rangle\cong-(E-E_c)\langle\phi_c|\phi_c\rangle, \quad (2.6)$$

TABLE I. Basis for the direct lattice. The atoms in the unit cell are located at $\pm(\frac{1}{4}a,0,\frac{1}{8}c)$.

Basis vector	(x,y,z)
t_1	$(a,0,-c)$
t_2	$(0,a,0)$
t_3	$(0,0,c)$

TABLE II. The reciprocal lattice. All coordinates are given in units of $(2\pi/a)$ $(a/c)=1.840$.

Basis vector	(G_x,G_y,G_z)
G_1	(2,0,0)
G_2	(0,2,0)
G_3	(1,0,a/c)
Symmetry point	
Γ	(0,0,0)
L	(1,0,0)
X	(0.5,0.5,0)
P	(0.5,0.5,0.92)
V	(0.5,0.0,0.92)
Special point	
W	(0,0,0.67)
H	(0,0,1.19)

[26] These values were extrapolated using the thermal-expansion coefficients from the *American Institute of Physics Handbook*, edited by D. E. Grey (McGraw-Hill Book Company, Inc., New York, 1963).

where ϕ_c is the part of ϕ in S^c, and E_c is a typical core energy. This quantity is so important that even in an orthogonalized-plane-wave (OPW) calculation, important errors may be caused by inexact knowledge of the core states $|b_t\rangle$, which does not allow the complete elimination of $|\phi_c\rangle$. In fact, the magnitude of (2.6) shows that the problem originates, not only in the overwhelming dissimilarity of the plane waves to the $|b_t\rangle$ outside the core regions, but equally in the rather large overlap of those plane waves with the core wave functions. This overlap is expressed by $\langle\phi_c|\phi_c\rangle$.

Before the pseudopotential equation is derived, we digress for an apology. It is hoped that the argument of the foregoing paragraphs has sketched the reasons why the Schrödinger equation

$$\mathcal{H}_0'|\phi\rangle=E\mathcal{P}_v|\phi\rangle \tag{2.7}$$

is used, with its modified Hamiltonian, when $|\phi\rangle$ is a sum of plane waves. While all this is very well known, it was felt that too much has sometimes been made of the arbitrariness of the pseudopotential as it is sometimes derived. It was felt not only that the difference between a good pseudopotential and a bad one is tangible, and ought to be understood, but also that the derivation of the appropriate form of the spin-orbit interaction (as shown in the next section) should be clearly free of any arbitrariness. Equation (2.7) can be expanded

$$\begin{aligned}\mathcal{H}_0'|\phi\rangle&=(1-\mathcal{P}_c)\mathcal{H}_0(1-\mathcal{P}_c)|\phi\rangle=\mathcal{H}_0(1-\mathcal{P}_c)|\phi\rangle\\&=E(1-\mathcal{P}_c)|\phi\rangle.\end{aligned} \tag{2.8}$$

Since an equation for the "pseudo wave function" $|\phi\rangle$ is being sought, we rewrite Eq. (2.8) as

$$\mathcal{H}_0|\phi\rangle+(E-\mathcal{H}_0)\mathcal{P}_c|\phi\rangle-(\mathcal{H}_0+V_R)|\phi\rangle=E|\phi\rangle, \tag{2.9}$$

where the new operator

$$V_R=\textstyle\sum_t(E-E_t)|b_t\rangle\langle b_t| \tag{2.10}$$

is an effective repulsive potential. This can be seen by looking at its diagonal matrix elements, which are positive. In the new secular equation (2.10) the matrix elements of the pseudopotential,

$$V_p=V+V_R, \tag{2.11}$$

are considerably smaller than those of V. The operator

$$\mathcal{H}^p=(1/2m)p^2+V^p=\mathcal{H}_0+V_R \tag{2.12}$$

is known as the pseudo-Hamiltonian.

If the fact that V_p is a nonlocal operator is overlooked, only the Fourier coefficients $V_p(\mathbf{G})$, for a few reciprocal lattice vectors $\mathbf{G}$, are of importance.

The approximation that V_p is simply a superposition of local, spherically symmetric atomic pseudopotentials $U(|\mathbf{r}|)$ has indeed proved quite successful in numerous energy-band calculations. Thus, energy bands in good quantitative agreement with experiment have been calculated with the use of as few as two or three coefficients $U(|\mathbf{G}|)$. The matrix elements of the pseudopotential in this approximation are

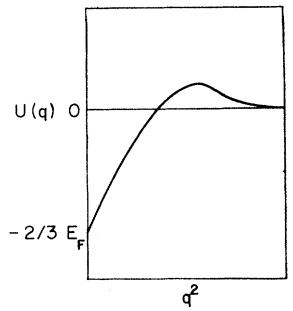

FIG. 3. Typical behavior of pseudopotential form factors.

$$\begin{aligned}\langle\mathbf{k}'|V_p|\mathbf{k}\rangle&=V_p(\mathbf{G})\delta_{\mathbf{k}'-\mathbf{k}-\mathbf{G}}\\&=U(|\mathbf{G}|)S(\mathbf{G})\delta_{\mathbf{k}'-\mathbf{k}-\mathbf{G}},\end{aligned} \tag{2.13}$$

where $\mathbf{G}$ is any reciprocal lattice vector, and the structure factor, normalized to unity, is

$$S(\mathbf{G})=(1/N)\sum_{j\text{ in unit cell}}e^{-i\mathbf{G}\cdot\mathbf{r}_j}. \tag{2.14}$$

The successful local-pseudopotential calculation of the band structures or Fermi surfaces of the elements above, below, and to the right of tin in the periodic table suggests that the use of this simple approximation would be successful in tin as well. The energy bands are determined by the form of $U(q)$. The general behavior of the curve of $U(q)$ as a function of q is shown in Fig. 3. In general there is a value q_0 such that, for $q>q_0$, $U(q)$ is very small and may be neglected. Thus, only four pseudopotential coefficients enter the present calculation; namely, U_1, U_2, U_3, U_4, which correspond to the reciprocal-lattice-vector types $G_1=(2,0,0)$, $G_2=(1,0,1)$, $G_3=(2,2,0)$, and $G_4=(2,1,1)$. While the U_i may be determined by fitting to empirical data, it is useful to have some starting point. Four available estimates of the U_i are listed in Table III.[27–30] It is to be noted that two of the estimates, one based upon extrapolation from Si and Ge, and the other based upon optical data, need a slight correction,[31] approximately 0.02 Ry for U_1 and U_2, to account for the fact that gray tin is a

TABLE III. Pseudopotential-form-factor estimates in rydbergs.

Source	$U1$	$U2$	$U3$	$U4$
Model potential calculation[a]	−0.126	−0.107	0.010	0.010
Model potential calculation[b]	−0.077	−0.058	0.038	0.055
Optical data[c]	−0.120	−0.085	0.050	0.055
Extrapolation from Ge and Si[d]	−0.170	−0.140	0.035	0.045
This calculation	−0.110	−0.060	0.030	0.020

[a] See Ref. 29. [b] See Ref. 30. [c] See Ref. 28. [d] See Ref. 27.

[27] P. J. Lin and L. M. Falicov, Phys. Rev. 143, 441 (1966).
[28] M. L. Cohen and J. K. Bergstresser, Phys. Rev. 141, 789 (1966).
[29] A. O. E. Animalu (unpublished).
[30] A. O. E. Animalu and V. Heine, Phil. Mag. 12, 1249 (1965).
[31] K. H. Bennemann, Phys. Rev. 139, A482 (1965).

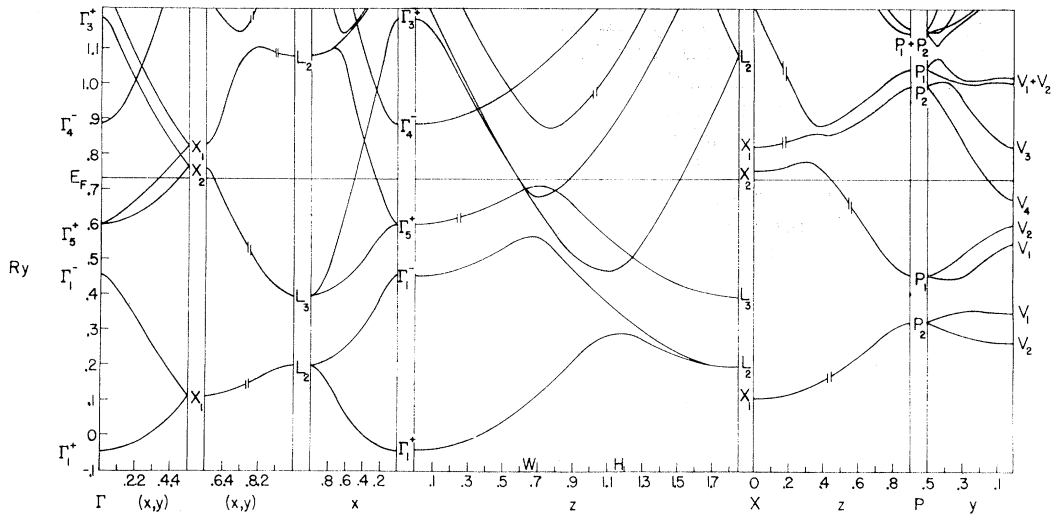

FIG. 4. The calculated energy bands of white tin without spin-orbit effects.

"covalent-bond" substance, while white tin is metallic. Nevertheless, the various sets of U_i are in disagreement among themselves. In fact, none of these sets of U_i gives good results in the present calculation. Then only the following general observations give us some guidance:

1. $|G_1|$ is close to $|G_2|$ and $|G_3|$ close to $|G_4|$, so that effectively only two averages values need be fitted initially;

2. Two quantities, U_2-U_1 and U_4-U_3, are between 0.019 and 0.035 Ry, and between 0.000 and 0.017 Ry, respectively. The values of the U_i arrived at by proper fitting and used in the present calculation are listed in Table III. The data used in the fitting are discussed in Sec. V of this paper.

C. Mechanics of the Calculation

In the neighborhood of each symmetry point, or other point of special interest, a plane-wave basis appropriate to that point was taken. A typical basis set numbered approximately 50 plane waves. In this way, good convergence was obtained, and there was no need for interpolation. The seemingly large number of plane waves required can be traced to three factors: the asymmetry of the lattice; the large Fermi sphere with eight electrons per unit cell; the size of U_1 and U_2.

The energy bands for the "empty lattice" case, $U(\mathbf{G})\equiv 0$, are shown in Ref. 32b, and the results of the present calculation are shown in Fig. 4, with the symmetry labels of Ref. 32a. Some gross effects that the lattice potential works upon the Fermi surface can readily be seen: the introduction of electrons along the W region of the ΓH line in zones 2, 3, and 4, and the removal of the electron regions of zone 5 at Γ and zone 6 at V. It will be noted that all of the energy levels on the XP and XL lines remain doubly degenerate. This degeneracy is preserved only at X and L, when spin-orbit effects are included. Since the Fermi surface is extremely close to X, the splitting of the stuck-together third and fourth bands must be quite small there, and magnetic breakdown[33] may be expected to occur at small or moderate fields. Therefore, it is certainly important to understand the effects of the spin-orbit interaction in this region. The spin-orbit coupling is also of interest in the neighborhood of the point W, where the spinless levels of zones 4, 5, and 6 are fairly close to each other and to the Fermi energy. Compared with this close energy spacing, the spin-orbit coupling is large. In the W region it certainly does not suffice to include this interaction as a perturbation.

III. SPIN-ORBIT COUPLING

The orthogonalized-plane-wave (OPW) method has proved to be accurate in calculating spin-orbit effects.[34, 35] It is the goal of this section to learn as much as possible from the experience of such calculations, and to apply this experience to the building of a model[36] compatible with the pseudopotential formulation. As the OPW formalism is closely related to the plane-wave pseudopotential formalism, there should be no difficulty in understanding the origin and nature of the spin-orbit matrix elements that arise in the latter.

[32] (a) M. Miasek and M. Suffczynski, Bull. Acad. Polon. Sci. Ser. Sci. Math. Astron. Phys. **9**, 477 (1961). (b) M. Miasek, *ibid.* **10**, 39 (1962).

[33] M. H. Cohen and L. M. Falicov, Phys. Rev. Letters **7**, 231 (1961).

[34] L. M. Falicov and M. H. Cohen, Phys. Rev. **130**, 92 (1963).

[35] L. Liu, Phys. Rev. **126**, 1317 (1962).

[36] A. O. E. Animalu obtains essentially the same result by a different approach (unpublished).

The spin-orbit Hamiltonian is

$$\mathcal{H}_s=(\hbar^2/4m^2c^2)(\nabla V\times\mathbf{p}\cdot\boldsymbol{\sigma}), \tag{3.1}$$

where V is the lattice potential, p is the momentum operator, and $\boldsymbol{\sigma}$ is the Pauli spin operator.

Let us denote spinors by capital letters. For example,

$$B_R=B_{ts}=b_t\uparrow,b_t\downarrow, \tag{3.2}$$

where in our notation s is the spin index, t are the core-function quantum numbers, (nlm), and s and t are combined in R. The spinors B_R are not necessarily the core eigenfunctions of the full Hamiltonian, but they are eigenfunctions of the spinless Hamiltonian $\mathcal{H}_0$, with the eigenvalues

$$E_R=E_{ts}=E_t. \tag{3.3}$$

It will be assumed here, as it is in the theory of atomic states, that the actual core functions are linear combinations, in spin space, of the no-spin core functions. Thus, the projection operator for the space spanned by the core states is

$$\mathcal{P}_c=\sum_R |B_R\rangle\langle B_R| = \mathbf{1}^{(s)}\sum_t |b_t\rangle\langle b_t|, \tag{3.4}$$

where $\mathbf{1}^{(s)}$ is the identity operator in spin space.

The Hamiltonian equation that corresponds to Eq. (2.8) is

$$(1-\mathcal{P}_c)(\mathcal{H}_0+\mathcal{H}_s)(1-\mathcal{P}_c)|\Phi\rangle=E(1-\mathcal{P}_c)|\Phi\rangle, \tag{3.5}$$

which, because of Eq. (3.4), immediately reduces to

$$\mathcal{H}^p|\Phi\rangle+(1-\mathcal{P}_c)\mathcal{H}_s(1-\mathcal{P}_c)|\Phi\rangle=E|\Phi\rangle, \tag{3.6}$$

where the $\mathcal{H}^p$ is precisely the pseudo-Hamiltonian of Sec. 2 multiplied by $\mathbf{1}^{(s)}$. Let us denote the matrix elements of the new operator by

$$\mathcal{H}_{\mathbf{k}'s',\mathbf{k}s}{}^{\text{s-o}}=\langle\mathbf{k}'s'|(1-\mathcal{P}_c)\mathcal{H}_s(1-\mathcal{P}_c)|\mathbf{k}s\rangle, \tag{3.7}$$

$$\begin{aligned}\mathcal{H}_{\mathbf{k}'s',\mathbf{k}s}{}^{\text{s-o}}=&\langle\mathbf{k}'s'|\mathcal{H}_s|\mathbf{k}s\rangle-\sum_R\langle\mathbf{k}'s'|B_R\rangle\langle B_R|\mathcal{H}_s|\mathbf{k}s\rangle\\&-\sum_R\langle\mathbf{k}'s'|\mathcal{H}_s|B_R\rangle\langle B_R|\mathbf{k}s\rangle+\sum_R\sum_{R'}\langle\mathbf{k}'s'|B_R\rangle\\&\times\langle B_R|\mathcal{H}_s|B_{R'}\rangle\langle B_{R'}|\mathbf{k}s\rangle.\end{aligned} \tag{3.8}$$

Terms such as these occur also in the OPW problem, so that the various existing OPW calculations may be used to justify some of the simplifying approximations which will presently be made. In these calculations it is found that, for states that contain an l symmetry already included in the core states, the double summation (the "core-core term") makes the largest contribution to (3.8). In magnesium,[37] for example, the core-core and core–plane-wave terms account for 99% or more of the contributions. Therefore, these are the terms which must be evaluated precisely. Because of the singularity of ∇V near the atomic nuclei, the largest contribution comes from these regions. Here, the overlap of core orbitals and potentials is negligible, so that in Eq. (3.8) all the matrix elements of $\mathcal{H}_s$ except the one between two plane waves are calculated using a spherically symmetric potential in each atomic cell. This allows $\mathcal{H}_s$ to be expressed as a sum of atomic Hamiltonians.

$$\mathcal{H}_s=\frac{1}{4mc^2}\sum_{\text{all atoms}}\frac{1}{|\mathbf{r}-\mathbf{r}_i|}\frac{dV(|\mathbf{r}-\mathbf{r}_i|)}{d|\mathbf{r}-\mathbf{r}_i|}\times\mathbf{l}(\mathbf{r}-\mathbf{r}_i)\cdot\boldsymbol{\sigma}, \tag{3.9}$$

where l is the angular-momentum operator.

If the core orbitals are expressed in the form

$$b_{nlm}(\mathbf{r})=R_{nl}(r)Y_l^m(\theta,\phi), \tag{3.10}$$

where the angular functions Y_l^m are the spherical harmonics, the matrix elements can now be calculated. This is done in the Appendix. The result, if as is the case in tin, the cores contain only s, p, and d states, is

$$\begin{aligned}\mathcal{H}_{\mathbf{k}'s',\mathbf{k}s}{}^{\text{s-o}}=&S(\mathbf{k}-\mathbf{k}')[(\hbar^2/4mc^2)U(|\mathbf{k}'-\mathbf{k}|)\\&-\lambda_1-\lambda_2(\mathbf{k}'\cdot\mathbf{k})]i\mathbf{k}'\times\mathbf{k}\cdot\boldsymbol{\sigma}_{s's}.\end{aligned} \tag{3.11}$$

The quantity S is the structure factor, U the Fourier transform of the crystal potential, and λ_1 and λ_2 positive constants that account for the contribution of the core p states and d states, respectively. The only approximations that have been made are Eq. (3.9) and, in the Appendix, a very accurate approximation, probably good to within 1% for p-like valence states and better for d-like ones. The term involving the crystal potential U accounts for the matrix elements of the original spin-orbit Hamiltonian between two plane waves. Consequently, as has been explained following Eq. (3.8), it only contributes 1% or less of the spin-orbit matrix element under typical conditions. If the atomic potentials were δ functions, this term could be exactly replaced by a change in λ_1. For actual lattice potentials, such an approximation results in an error of about 30% of the original small value, which was about 1% of the main contribution. The other relativistic corrections can be thought of as equivalent k-dependent pseudopotentials. Therefore, since we determine our pseudopotentials empirically, these corrections are automatically included in the model as described in the last section.

In tin, the energy levels for which the spin-orbit interaction concerns us are expected to be p-like, so that we set $\lambda_2=0$. The value of λ_1 was arrived at in the following fashion. It has been found that the spin-orbit splittings for the valence electrons in a solid tend to be close to the corresponding atomic values. Thus, the spin-orbit splitting of the low-lying p-like states at the symmetry point Γ should most closely resemble that of the s^2p ground state of the singly ionized tin atom. The experimental value for the atomic case[38] is 0.039 Ry. The assumption that this value ΔE_{atom} is essentially unchanged in the solid is borne out by the OPW calculation of the spin-orbit splittings for gray

[37] L. M. Falicov (private communication).

[38] *Atomic Energy Levels*, edited by C. E. Moore, Nat. Bur. Std. Circ. No. 467 (1949).

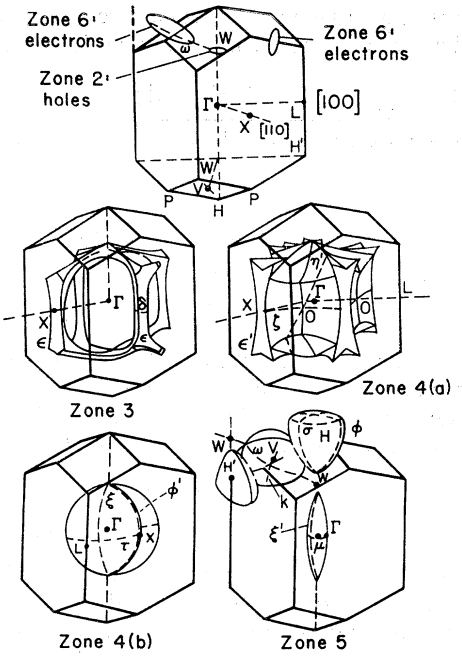

FIG. 5. The Fermi surface of tin on the nearly-free-electron model.

tin.[39] There it is calculated that the relevant Γ_{25}' and Γ_{15} levels, which belong to p-bonding and p-antibonding states are split by 0.0439 and 0.0362 Ry, respectively. The average of these can be seen to be close to ΔE_{atom}; therefore it seems reasonable to expect the splitting to be approximately the same in white tin. However, because of the asymmetry of the tin lattice, the p_x and p_y states which comprise Γ_5^+ are 0.652 Ry below the next p_z state, Γ_3^+, in the empty-lattice case. Therefore, there is essentially no spin-orbit interaction of the p_x and p_y states with the p_z state. By assuming that the spin-orbit matrix elements between the Γ_5 states are the same as those that lead to the value ΔE in the atom and in gray tin, one finds that the Γ_5 states should be split by $\frac{2}{3}\Delta E$, or 0.026 Ry. This can be accomplished by setting $\lambda_1=0.0019$ Ry, where it should be remembered that the propagation vectors $\mathbf{k}$ are measured in units of $(2\pi/a)$.[40]

How the closely spaced energy levels at a point near W varied when the spin-orbit coupling strength λ was varied is shown in Table IV. The strong effect of the actual spin-orbit coupling in a region around an accidental degeneracy can be seen in Fig. 6. At typical places in the zone, the effect of the spin-orbit coupling was negligible, and the no-spin calculation was adequate. At X, a location of particular interest, the energy levels do not split, but there is a shift of -0.0027 Ry for the third and fourth bands. Of course, as is required by group theory, there is no splitting of levels either at X or at L. The splitting at the third and fourth bands at the Fermi energy is 0.0013 Ry on the XL line, and 0.0041 Ry on the XP line. This corresponds to magnetic breakdown at fields of the order of 4000 G along the c axis.

TABLE IV. The effect of λ on the energies at $(0,0,0.625)2\pi/a$. Energies are in Ry.

λ	Zone 3	Zone 4	Zone 5	Zone 6
0	0.6995	0.6995	0.7002	0.7083
0.00095	0.6812	0.7002	0.7112	0.7126
0.0019	0.6914	0.7007	0.7066	0.7100
0.0038	0.6601	0.6997	0.7159	0.7246

[39] F. Bassani and L. Liu, Phys. Rev. 132, 2047 (1963).
[40] $\lambda=0.0016\times10^{-16}$ Ry cm^2.

IV. THE FERMI SURFACE

Until now, experiments on the Fermi surface of tin have usually been compared with the nearly-free-electron (NFE) model.[1] Most of the actual Fermi surfaces of tin are recognizable distortions of this model. The NFE surfaces are shown in Fig. 5.

In zone 2, there are small pockets of holes around the points W. In zone 3, the surface contains a multiply connected network of cylinders, consisting of holes. Zone 4 contains a multiply connected hole-type sur-

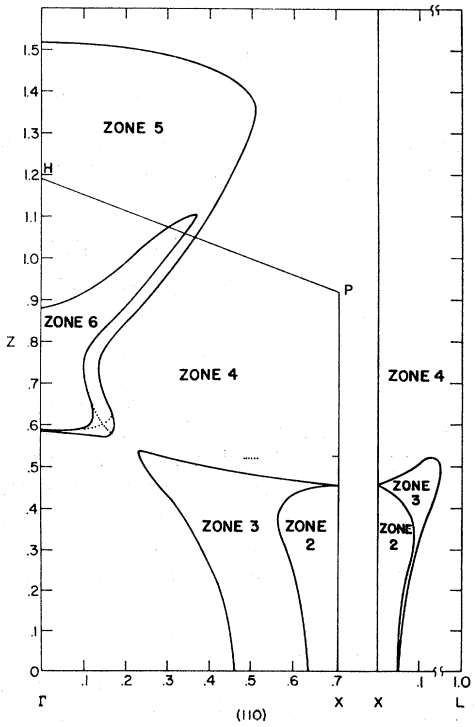

FIG. 6. The ΓXP plane, and the third- and fourth-zone contours in the PXL plane. The intersecting dotted lines show the energy surfaces when the spin-orbit interaction is ignored. The other dotted lines are portions of the projection of the ridges of the fourth-zone sheet. A zone number in any region indicates the highest zone containing electrons there. Thus, the nth zone Fermi surface separates the regions marked n and $n-1$.

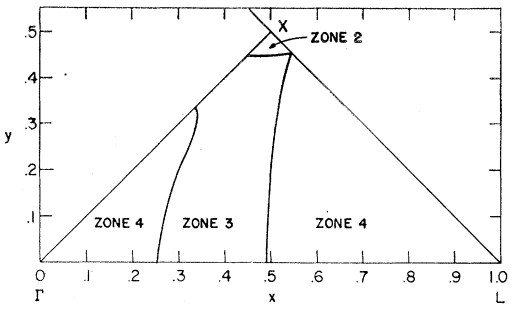

FIG. 7. The Fermi surface contours in the ΓXL plane. The notation is the same as in Fig. 6.

face 4(a) and a crossed pair of electron "pancakes" along the ΓXP (110)-type planes. Zone 5 has two electron-like surfaces, the first consisting of vertical cylinders centered on Γ, and the second a large multiply connected sheet, usually thought of as consisting of "pears" and "connecting pieces." The tapered end of a "pear," near the point W, will be called the tip, and the flat end the top. The top is roughly square, with its edges along the (100)-type directions. The "connections" are centered on the point V, and extend in the (100) directions to connect a top-up pear with a top-down pear. Their cross section is in the shape of a four-pointed star, with the distance between the points narrowing in the direction of the pear tip to which they are attached. The electrons in zone 6 are contained in a cigar-shaped piece around the point V, and in four cigar-shaped pieces starting near the point W and extending toward the corners of the pear tops.

According to the present calculation, the crystal potential modifies the NFE Fermi surfaces as follows. The zone-2 hole surface at the point W disappears. In zone 3, the hole cylinders extending from W are destroyed, leaving only the cylinders along the XP lines, as is shown in Fig. 6. In zone 4, electrons are introduced along ΓH near W, so that there is a region, to be called the "neck," connecting the electrons of 4(b) with the electrons outside 4(a), as is illustrated schematically in Fig. 8. See also Figs. 6, 7, and 9 for cross sections. In zone 5, the cigar around Γ disappears, and the pear network remains essentially unchanged. It is schematically illustrated in Fig. 10, while some cross sections of it may be found in Figs. 6, 9, and 11. In zone 6 the piece around the point V disappears, while the "cigars" near the points W are amalgamated into a vertical shape of square cross section (Figs. 6 and 9) with slight prongs in the directions of the original "cigars." With the magnetic field B parallel to the (100) direction, there are, according to the calculation, open orbits on zone 5 as well as a very narrow band of them on zone 4. With **B** parallel to (110), the calculation predicts open orbits on zone 5, but, because of the presence of the neck, not on zone 4.

V. COMPARISON WITH EXPERIMENT

In this section we compare the results of the calculation with the available experimental information. The various relevant experiments are discussed; the data used in the determination of the fitting parameters are explicitly shown. The quantitative agreement between the calculation and the experimental data is shown to be excellent throughout, except in the sixth zone, and in a small region of the fifth zone, where the agreement is only fair.

A. Size Effect

The cyclotron size-effect experiment of Gantmakher[6,7] is outstanding for its convenience of interpretation, its accuracy, and the wealth of information it contains. A magnetic field B is applied parallel to the surface of a thin plate. If the electron mean free path is long enough, the surface impedance, measured at anomalous skin-effect frequencies, shows singularities at certain magnetic fields; namely, the magnetic fields at which certain extremal electron orbits fit perfectly across the plane (see Fig. 12). If the normal to the surface is **n**, the experiment measures the caliper ($2p$ in Fig. 12) of an orbit in the $\mathbf{n}\times\mathbf{B}$ direction in momentum space. The orbits may be extremal in possessing the smallest or largest caliper in their vicinity. Sums of calipers may also be measured, for favorably shaped Fermi surfaces. In this effect, extremal electrons accelerated at one boundary of the plate set up intense current sheets in the interior. Thus a whole chain of orbits may be detected. Gantmakher reckons his experimental error to be about 2–3%, in addition to an ambiguity sometimes as much as 5%, due to the lack of any theoretical model for the line shapes of the size-effect experiment. Figure 13 exhibits Gantmakher's results for different planes of rotation of the magnetic field. These figures will also be referred to as G^1, G^2, and G^3. Thus, the

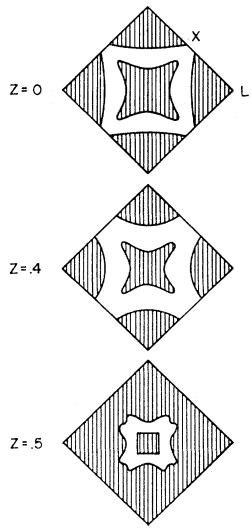

FIG. 8. Schematic cross sections of the fourth zone in several planes perpendicular to the c axes at various heights. The electron regions are shaded.

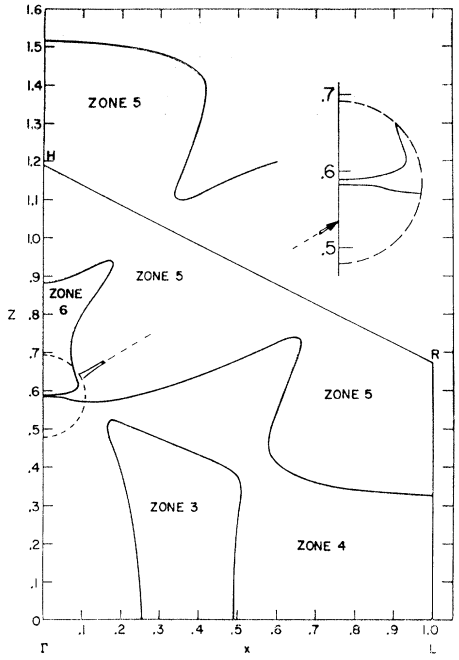

FIG. 9. The Fermi surface contours in the ΓLR plane. The notation is the same as in Fig. 6.

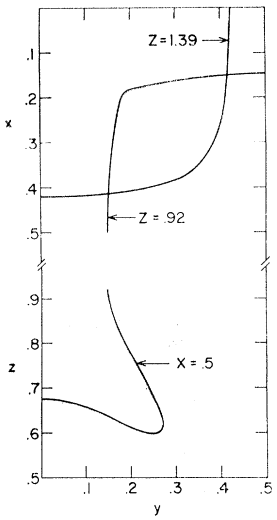

FIG. 11. Fifth-zone Fermi energy contours in the (x,y) planes at $z=1.39$ and $z=0.92$, and in the (z,y) plane at $x=0.5$. For schematic diagrams of the $z=1.39$ and $z=0.92$ contours, see the lower and upper portions of Fig. 10. The $x=0.5$ contour is part of the star-shaped contour of the fifth-zone connecting piece, midway between a tip-up pear and a top-up pear.

appropriate curve numbered 5 will be referred to as $G^{1}5$. Note that the directions indicated on these diagrams represent the directions of the semicalipers in momentum space. Tables V–VIII compare the size-effect extremal semicalipers with the calculated ones.

The curve $G^{1}1$, for the orbit ζ, resembles the predictions of the free-electron model extremely well. The deviations amount to approximately $0.01(2\pi/a)$, which is within experimental error. But $G^{1}1$ as well as the calculation definitely show a reduced curvature for $\theta=0°$ (Fig. 13). The extreme flatness of the Fermi surface at the point 0 (Fig. 5) makes it possible to observe chains of orbits ζ. The curve $G^{2}1$ also measures ζ, with a caliper close to the free-electron model. Curve $G^{1}11$ [Fig. 14(e)], which comes from an orbit over two pears, is also close to its nearly-free-electron-model value. Both the curves $G^{1}4$ and $G^{1}5$ measure the width of the neck of zone 4, at different field directions. In G^{2}, the vertical columns of zone 3 can be seen. Note that the maximum calipers for the (110)-type directions are seen at two different field directions, so that the bottoms of $G^{2}10$ and $G^{2}11$, when translated vertically, fit the bulge near the top. Only one of the calipers of the smallest orbit is perhaps detected experimentally. The curves $G^{1}6$ and $G^{2}6$ go up to the approximate height and angle given by the calculation, which is determined roughly by the location of the pear tips, but the experimental curves start ($\theta=90°$) at a value smaller than the theoretical one. In the light of the present calculation, curve $G^{1}14$ cannot be the caliper of a single orbit. It is in fact twice the caliper $G^{1}9$, which is due to orbits over the ridges of the zone-4 Fermi surface. Both the possibility of $G^{1}14$ and the flatness of the $G^{1}9$ and $G^{1}14$ curves stem from the circumstance that a large number of zone-4 orbits have approximately the same caliper in

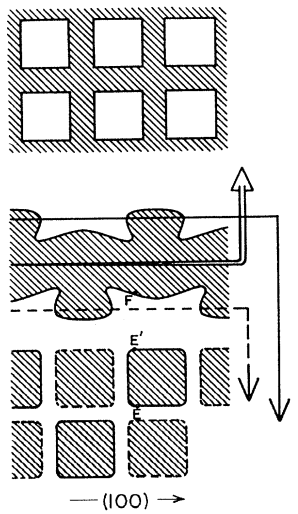

FIG. 10. Schematic diagram of cross sections of the fifth-zone electron regions. The cross sections by the ΓLR plane (middle diagram), and cross section in two horizontal planes (upper and lower diagrams). The electron regions are shaded.

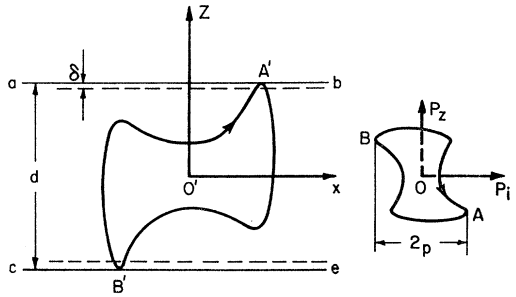

FIG. 12. Electron trajectory in momentum space (right) for the size effect, and the corresponding orbit in real space. The magnetic field is perpendicular to the plane of the drawing: *ab* and *ce* are boundaries of the sample.

TABLE V. Semicalipers for **B** in the [001] direction.

G Figure	Curve No.	Expt.	Calc.	Zone	Label	Description
1	1	0.515	0.51	41	ζ	$z=0$
1	2	0.35	0.35	5	Fig. 13	$z=0.92$
1	3	0.4	0.42	5	σ	Pear crown
1	4	0.305	0.34	4	τ	$z=0$
1	15	0.19	0.17	4		Neck
2	2	0.43	0.46	4	τ	$z=0$
2	1	0.66	0.66	4	ζ	$z=0$
1	12	0.1	0.177	6		Smallest orbit
2	10	0.125	0.145	3		Greatest orbit
2	11	0.093	0.087	3		Greatest orbit
2	12	0.083	0.07	3		Largest caliper of smallest orbit

the [001] direction. (See the horizontal dotted lines in Fig. 6.) Curve $G^3 2$ gives an experimental picture of the pear top (see calculation in Fig. 11), and $G^3 5$ shows how the points of the corresponding star-shaped connections narrow as they near the tip of the next pear. Both $G^3 5$ and a section of $G^3 10$ ($\alpha<10°$) were

TABLE VI. Semicalipers for **B** in the [100] direction.

G Figure	Curve No.	Expt.	Calc.	Zone	Label	Description
1	5	0.20	0.21	5	Fig. 11	Open orbit, $y=0$
1	6	0.25	0.32	5	Fig. 15	$y=0.5$
1	7	0.425	0.45	5	Fig. 12, $\sim EE'F$	$y\sim 0.35$
3	2	0.405	0.42	5	Fig. 11	Open orbit, $y=0$
3	6	0.547	$\sim$0.53	4		$y\sim 0.2$
3	1	0.176	0.18	6		$y=0$
3	11	1.02	$\sim$1.04	5		Open orbit, $y=0$
1	9	0.51	$\sim$0.525	4	Like ϵ' and η'	See dotted lines on Fig. 6
1	14	1.05	$\sim$1.05	4		Double the foregoing orbit[a]

[a] Most of the orbits on the zone-4 Fermi surface have calipers between 0.52 and 0.53, as can be seen from the relevant horizontal lines in Fig. 6.

seen only when the component of the electric field parallel to the magnetic field was nonzero, as should be the case for orbits at the extremal point of which the electron has a large velocity in the magnetic-field direction. This is in accord with the identification of these orbits. Note that the data of $G^1 1$ and $G^3 10$ make it

TABLE VII. Semicalipers for **B** in the [110] direction.

G Figure	Curve No.	Expt.	Calc.	Zone	Label	Description
2	3	0.195	0.1975	5		Fig. 21(b) incomplete orbit through (0.35,0.0,1.1)
2	6	0.25	$\sim$0.32	5		Inner caliper from extended orbit near preceding orbit
2	7	0.42	0.475	5	ϕ	Fig. 8, $x=y$
2	9	0.49	0.52	4		Fig. 20(d)
3	2	0.466	0.51	5	ϕ	Fig. 8, $x=y$
3	3	0.426	0.485	5		Fig. 20(a), near $x=y+0.125$.
3	1	0.27	0.37	3		$x=y$

impossible for more than a narrow strip of open orbits to exist on the fourth zone in the (100) direction, with B in the (010) direction. Curves $G^3 2$ and $G^3 11$ come from the same open orbit in zone 5, and cumulative calipers should be observed [Fig. 14(k), (l)]. Gantmakher sees them in Ref. 8. There he also identifies such a series of two types of cumulative calipers in the (110) direction.

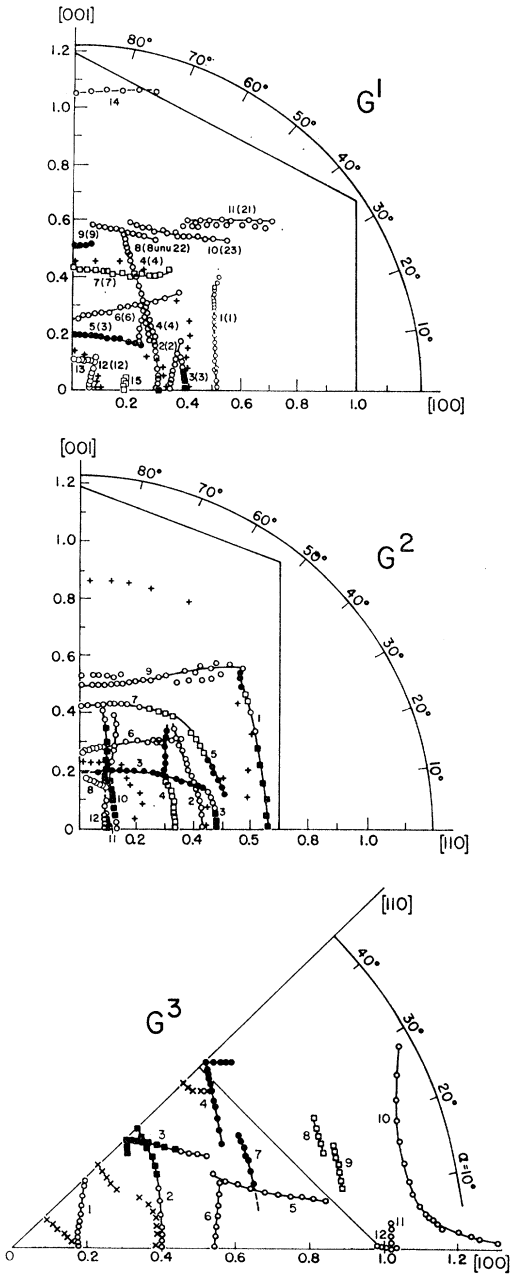

FIG. 13. Gantmakher's experimental semicalipers in the (010) [Ref. 6], (1$\bar{1}$0) [Ref. 6], and (001) [Ref. 7] planes. The different symbols denote different experimental line shapes. The light continuous lines are the central cross sections of the Brillouin zone. The x's are the magnetoacoustic data of Ref. 13. The axes of the bottom figure should be interchanged for the magnetoacoustic data.

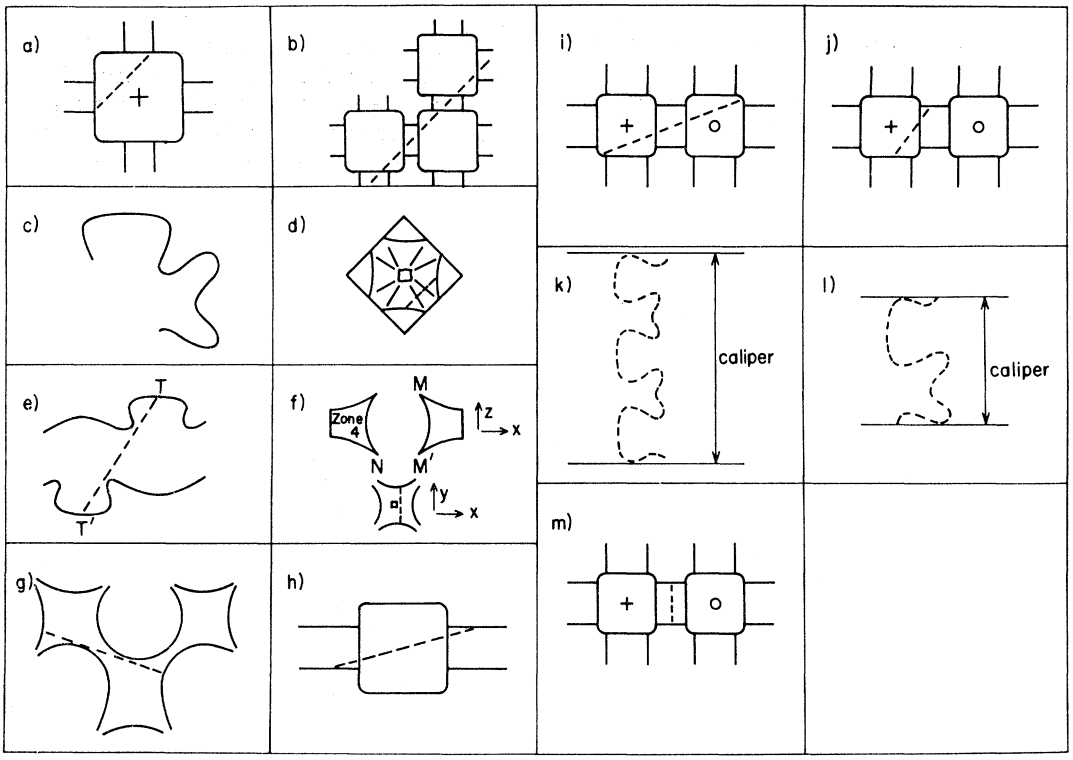

FIG. 14. Sketches of electron orbits (dotted lines, if any) on the Fermi surface. A top-up pear is indicated by a +, a tip-up pear by a O. All orbits shown come from the fourth-zone multiply connected sheet [(d), (f), and (g)] or the fifth-zone multiply connected sheet. Cumulative calipers are shown in (k).

In Ref. 7 he identifies $G^3 3$ and $G^3 4$ as coming from open orbits. The natural assumption that the two calipers of Ref. 8 are the $G^3 3$ and $G^3 4$ of Ref. 7 is contradicted by the estimate[41] that their ratio is ≈ 0.5, in Ref. 8, whereas the ratio is 0.68, in Fig. 13. Although the width of the line shape is considerable in the relevant experimental graph of Ref. 8, it does not, seemingly, suffice to explain the discrepancy. If there is such a discrepancy it may be explained by our interpretation of $G^3 3$ as the orbit of Fig. 14(a), near $x=y+0.125$. When, instead, cumulative calipers are observed, they depend on a region of open orbits centered on the $x=y+0.25$ orbits [Fig. 14(b)]. A number of orbits around that of Fig. 14(a) are filtered out in the cumulative case, so that if a broad strip of orbits with a range of calipers were originally involved, the position of the experimental line could certainly shift. In our understanding of the experiment, a highly convoluted periodic open orbit, for example the one in zone 5 in the (100) direction, $G^3 11$, should exhibit calipers somewhat larger than its period [see Fig. 14(l)]. This seems to be confirmed in $G^3 11$ and $G^3 4$. In other words, the relevant cumulative calipers in such a case should be given by the formula

$$D=nD_0+\delta, \tag{5.1}$$

where n is an integer, D_0 is the actual period of the orbit, and δ represents the amount of the backwards convolution. In Ref. 8 the D_0 in Eq. (5.1), for the (100) and (110) open orbits was found to be 2–3% larger than the corresponding periods of the reciprocal lattice. This was attributed to an error in sample thickness. It would be interesting to perform a careful test to see if Eq. (5.1) holds for $G^3 11$, since our calculation predicts that δ is 4% of D_0, and thus should be observable. If Eq. (5.1) does hold, it could be used to determine the sample thickness precisely, and eliminate it as a source of error for the G^3 curves.

[41] This is the estimate of Ref. 8 and also the appearance of the relevant data graph in Ref. 8.

B. Cyclotron Resonance

We now discuss the cyclotron-resonance experiments that have been performed on tin. In contrast to the size-effect experiment, the results here are less convenient to interpret quantitatively. We point out a few interesting data.

The cyclotron masses found by Khaikin[9] will be denoted by the number he has given to them (Fig. 4, Ref. 9) and the letter K. The magnetic field ranges over the same directions as in the G^1 and G^2 data diagrams. In Ref. 9 the observation is made that the existence of a surface such as the free-electron surface of zone 4b would have given rise to sharp resonances which could have been observed at all angles, and which were not, in fact, observed. The τ orbit does give rise to a sharp

TABLE VIII. Selected semicalipers for **B** in general directions.

G Figure	Curve No.	Location on expt. figure	Quantity	Expt.	Calc.	Zone	Description
1	11	$x=0.5$	z	0.6	0.6	5	TT' in Fig. 12, Fig. 20(e)
1	8	z axis intercept	z	0.6	0.535	4	Fig. 20(f) (MM')
1	10	z maximum	z	0.6	0.535	4	Fig. 20(f) (MN), symmetric about Γ
3	10	$\alpha=10°$	Magnitude	1.08	1.11	4	Fig. 20(g), through XP line
3	5	$x=0.5$	z	0.24	0.27	5	Fig. 20(h), one pear and two connections
3	9	$\alpha=10°$	Magnitude	0.91	0.94	5	Fig. 21(a), two pears

resonance $K4$, which is cut off by the neck, at 70° on the diagram, as compared with 72° for G^14, and 72° maximum for the calculation. $K9$ can then be identified with the "earring" orbit through the neck. $K1$ corresponds to G^11, the ζ orbit. $K8$ is the fifth-zone orbit around the connecting piece, Fig. 14(m), as will be argued presently. Cyclotron resonance experiments[10,11] have been performed in slightly nonparallel fields, and in field directions normal to the surface (the so-called Galt configuration). In both cases the magnetic field was in the (100) direction, or near it. In Ref. 11 a mass $m^*=0.49m_e$ was found to belong to a noncentral extremal cross section, such that it has a large velocity in the (100) direction over a part of its orbit. This is the mass $K8$ that has been identified as belonging to the fifth-zone connecting pieces. Koch and Kip,[10] using the Galt configuration, obtain a mass of $0.57m_e$ which is only seen when the electric field is in the (100) direction. This is the result that would be obtained from a cylindrical Fermi surface tilted between the (100) and the (001) directions. Again, the description fits the connecting pieces, and the fifth zone must certainly be responsible. It would be interesting if both masses were detected by the same experiment. However, at present we can only suggest one location on the Fermi surface. Koch and Kip also found masses of $0.2m_e$ and $0.3m_e$ for an electric field polarized in the (001) direction. This configuration is good for detecting Fermi-surface cylinders tilted between (110) and (010). Only the third and fourth zones in the region of the XP lines fit this description.

C. de Haas–van Alphen Effect

A number of de Haas–van Alphen periods and cyclotron masses have been obtained by Gold and Priestley[1] (referred to here as GP). It is unfortunate that the experimental errors were considerable for the large areas, while the small areas cannot be expected to be too accurate in the calculation. Table IX lists the major de Haas–van Alphen periods that we have calculated. Diagrams in Ref. 1 show the de Haas–van Alphen periods (referred to by capital letters) in the major planes, as well as the amplitude variation for **B** in the (100) plane. The amplitude dependence of the oscillations K is striking, so that we recognize the zone-4 earring orbit immediately. K is extinguished at $17\frac{1}{2}°$, as compared with the 20° upper bound from Ref. 9, the 18% upper bound from Ref. 6, and 18% from the calculation. The period of the oscillation K is in fair (10%) agreement with the calculation. The effective mass of $0.5m_e$ agrees with Khaikin's value, $0.53m_e$, for $K9$. The curve H is consistent with the angular dependence that the orbit about the fifth-zone connection should have. The fact that H is 30% too large is in good agreement with Gantmakher's experiment, since, according to our interpretation of the latter, our theoretical horizontal caliper is 12% too large, and our vertical caliper 28% too large. Gold and Priestley's mass, $0.45m_e$, agrees with the mass $m^*=0.49m_e$ that Khaikin[11] has obtained with a slightly skew magnetic field. Since Gold and Priestley claim 10% accuracy for the masses, their measurement is also in agreement with the $m^*=0.57m_e$ of Koch and Kip. The period CC' has the proper angular dependence for the sixth-

TABLE IX. Calculation of de Haas–van Alphen periods.

Zone	Period (G^{-1})	Gold and Priestley	Description
		B‖[001]	
3	8 $\times10^{-7}$		Basal plane
	3.3 $\times10^{-7}$	B2.85$\times10^{-7}$	Maximum area
4	2.32 $\times10^{-8}$	E2.8 $\times10^{-8}$	τ
	8.39 $\times10^{-9}$		ζ
	6.38 $\times10^{-8}$		Neck
5	1.23*$\times10^{-8}$		σ
	1.76 $\times10^{-8}$		(Fig. 13) surrounded by 4 pears, 4 connections.
6	3.54 $\times10^{-7}$		Smallest area
	6.15 $\times10^{-8}$		Around the bulge, near the spikes
3–4	0.746$\times10^{-8}$		ζ orbit with magnetic breakdown to zone 3
		B‖[110]	
3	7.4 $\times10^{-8}$		Zone face
	4.31 $\times10^{-8}$		ΓXP plane
4	4.38 $\times10^{-8}$		Zone face
	1.14 $\times10^{-8}$		ΓXP plane
5	~1.3 $\times10^{-8}$		Central orbit including spikes, ±10%
		B‖[100]	
4	3.18 $\times10^{-8}$	K2.86$\times10^{-8}$	Earring
	~0.8 $\times10^{-8}$		Largest area
5	3.63 $\times10^{-8}$	H4.7 $\times10^{-8}$	Fig. 15, orbit about connection
6	1.43 $\times10^{-7}$	2.1 $\times10^{-7}$	Fig. 11

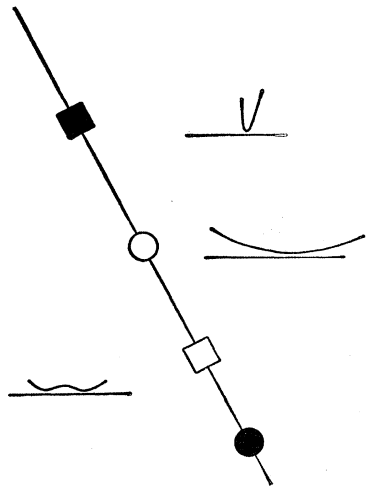

FIG. 15. Line-shape symbols used by Gantmakher [Ref. 6] together with kinds of orbits to which they may correspond.

zone surface, and is once more in good agreement with Gantmakher. According to the latter ($G^1 13, G^3 1$), our calculated area should be in error primarily because we overestimate its height by 28%. We do, in fact, overestimate the area by 23%. The effective masses $0.26m_e$ for C and $0.34m_e$ for C' identify CC' with Khaikin's $K9$ [$0.27m_e$ at (100) and $0.37m_e$ at (110)] as zone 6. The effective masses of GP and of K are in agreement with the essentially square (001) cross sections and slight spikes of the sixth zone. The curve B certainly has the angular dependence that an orbit on the knobs of the zone-3 cylinders should have. That is, the area increases slowly as the magnetic field B is tilted away from (001). Its area is 14% less than the calculated one.

Note in the amplitude diagram of GP that the maximum in B at 40° is to be expected, when, at some magnetic-field inclination, the B orbit slides down to meet the symmetric orbit centered on the point X. The bump on the E-amplitude curve may also correspond to a coalescing of two extremal areas. The curve $G^1 4$ coalesces with a companion curve in this very interval. The orbit in question is τ, and the angular dependence of the period B is the correct one [slow decrease with tilting from (001)]. The calculation is 18% away from the experiment. Again, the mass of GP, $0.51m_e$, agrees roughly with that of Khaikin, which is $0.43m_e$.

We remark in passing that Miller,[14] in a magnetoacoustic-attenuation experiment with $\mathbf{B}\|(001)$ has found two de Haas–type oscillations, one corresponding to GP's oscillation A, the other having a very long period, around 10^{-5} G^{-1}. We have no such area, but it might arise, for instance, from the spikes in zone 6, in a more accurate calculation.

D. Other Experiments

The magnetoacoustic-effect experiments will not be discussed in detail. The data from the best such experiment[13] giving calipers has been included by Gantmakher in our Fig. 13. The resemblance of the magnetoacoustic calipers to the size effect ones is often clear, but the accuracy of this type of experiment cannot compare with that of the size effect. Nor is the interpretation of the calipers as free from ambiguity. The magnetoacoustic effect has also been used to observe open-orbit resonances[12,15] in tin. The study of the general open-orbit topology of tin was done by the galvanomagnetic-effect study of Ref. 2. There it was shown that there exists a two-dimensional region of open orbits (see Ref. 2). In the past this region has been accounted for by nearly-free-electron-like fourth-zone surface. Not surprisingly, this is also in agreement with the present calculation. Measurements of the magnetoresistance have also been used[4] to observe an effect which is due to magnetic breakdown between the third and fourth zones, near the symmetry point X.

E. Other Considerations

Finally, we consider the line shapes that characterize the singularities which Gantmakher has obtained, in the size-effect experiment. The quantity he measured was the derivative of the surface reactance with respect to the magnetic field. He classified the line shapes into four kinds, denoted by solid or empty circles or squares in the graphs of his results. The search for a pattern in the occurrences of the various line shapes was taken up for the following reasons:

1. The size-effect experiment would become more valuable if information could be gotten from the line shapes.
2. Possible theoretical calculations of the line shapes could be checked conveniently.
3. If a rule were found, it might actually serve as a guide in a model calculation.
4. Any such pattern in the line shape could be used as a check on our assignments of calipers.

Guessing a rule from the "pattern" of a few data is, however, a precarious undertaking. There are too many variables that could easily be influential.

Thus, the pattern we have found is to be taken as a suggestion or speculation. We have noticed that when the line shape changes for any of the calipers, it is always adjacent to one that is its neighbor in Fig. 15. This whole pattern is included in the curve $G^2 1$. Two quantities that could vary continuously in this way are the shape of a single orbit, and the curvature of the calipers as the projection of the momentum on the direction of the magnetic field is varied. Concentrating on the former possibility, a pattern does seem to exist. We show our guess in Fig. 15. The line shape of the solid squares represents pointed orbits; that of the open circles, gently curved convex orbits; that of the open squares, slightly concave orbits with two points of contact that are not too pronounced; that of the solid

circles at least predominantly with open orbits whose opposite extremes are dissimilar in flatness, or not very flat. This kind of scheme would, for instance, cast doubt upon our assignment of $G^2 12$ (although here the proximity to $G^2 11$ might make the line shape unreliable as a guide), which we attribute to the largest caliper of the smallest orbit on zone 3.

In addition to the pseudopotential coefficients, the Fermi energy was used as a fitting parameter, for practical reasons, and finally set equal to 0.730 Ry. The experimental parameters used for the determination of the pseudopotential coefficients were:

1. the height of the pear top, derived from $G^1 11$;
2. the location of the large, flat portion of the fourth zone, derived from $G^1 1$;
3. the size of the star-shaped fourth-zone orbit in the basal plane, determined from $G^1 4$ and $G^2 2$;
4. the size of the fourth-zone neck, determined by $G^1 15$ and $G^1 4$, as well as the height of the neck;
5. the supposed size of the smallest orbits of the third zone.

Some of these Fermi-surface parameters were in conflict with each other: 3 and 5, for example. One of the good features of the pseudopotential technique is that the particular form of the secular equation is a strong condition which does not allow, for reasonable pseudopotentials, as much arbitrariness as the number of fitting parameters would suggest.

VI. DISCUSSION

The local-pseudopotential approximation has been found to be adequate for white tin. The main effect of the pseudopotential is to change the nearly-free-electron model so as to eliminate the holes in zone 2, and the electrons in zone 5 at Γ and zone 6 at V, and to spread the surfaces apart at W.

In the OPW calculation of Ref. 42, self-consistency was simulated by choosing the value of a certain parameter $V(0)$ so as to cause the zone-5 surface to exist in the neighborhood of Γ. The existence of this surface was considered to have been conclusively demonstrated by experiment. However, this is not so, and therefore we think that Ref. 42 is in error. The present paper shows some minor quantitative discrepancies with experiment in the fifth and sixth zones. It is also not free of the possibility of error in the assignment of the experimental data to theoretically calculated values. However, the over-all agreement is quite satisfactory and it is expected that the use of more pseudopotential coefficients would improve the agreement.

This calculation has given us a detailed picture of the Fermi surface. It has also proved the possibility and convenience of including the spin-orbit interaction in the pseudopotential formalism in a general way. This is of the utmost importance in the study of the electronic properties of heavy elements like lead[22] and bismuth.[43]

ACKNOWLEDGMENTS

The author is deeply indebted to Dr. L. M. Falicov for suggesting the problem, for his supervision of it, and most of all, for his example. The author would also like to express his gratitude to Miss Lucia Crossman and Miss Dianne Berger, for their generous help under trying conditions.

The research benefited from general support of the Institute for the Study of Metals by the Advanced Research Projects Agency and the National Science Foundation.

The computations were done on the 7094 computer at the University of Chicago Computation Center.

APPENDIX: SIMPLIFICATION OF THE SPIN-ORBIT MATRIX ELEMENTS

Summing on the spin indices in (3.8), we obtain

$$\begin{aligned}\mathcal{H}_{\mathbf{k}'s',\mathbf{k}s}{}^{s-o}=&\langle \mathbf{k}'s'|\mathcal{H}_s|ks\rangle-\textstyle\sum_R\langle \mathbf{k}'s'|B_{R'}\rangle\\ &\times\langle B_{R'}|\mathcal{H}_s|\mathbf{k}_s\rangle-\textstyle\sum_R\langle \mathbf{k}'s'|\mathcal{H}_s|B_R\rangle\langle B_R|\mathbf{k}s\rangle\\ &+\textstyle\sum_R\sum_{R'}\langle \mathbf{k}'s'|B_{R'}\rangle\langle B_{R'}|\mathcal{H}_s|B_R\rangle\langle B_R|\mathbf{k}s\rangle. \quad \text{(A1)}\end{aligned}$$

Simplifying, and introducing the notation

$$\mathcal{H}_s=\mathbf{\Lambda}\cdot\boldsymbol{\sigma}, \quad \text{(A2)}$$

gives

$$\begin{aligned}\mathcal{H}_{\mathbf{k}'s',ks}{}^{s-o}=&\langle s'|\boldsymbol{\sigma}|s\rangle\cdot\{\langle \mathbf{k}'|\mathbf{\Lambda}|k\rangle-\textstyle\sum_t\langle \mathbf{k}'|b_t\rangle\langle b_t|\mathbf{\Lambda}|\mathbf{k}\rangle\\ &-\textstyle\sum_t\langle \mathbf{k}'|\mathbf{\Lambda}|b_t\rangle\langle b_t|\mathbf{k}\rangle+\sum_t\sum_{t'}\langle \mathbf{k}'|b_{t'}\rangle\\ &\times\langle b_{t'}|\mathbf{\Lambda}|b_t\rangle\langle b_t|\mathbf{k}\rangle\}\\ =&\langle s'|\boldsymbol{\sigma}|s\rangle\cdot\{\mathbf{\Lambda}^{pp}+(\mathbf{\Lambda}^{pc}+\mathbf{\Lambda}^{cp}+\mathbf{\Lambda}^{cc})\\ &\times S(\mathbf{k}-\mathbf{k}')\}, \quad \text{(A3)}\end{aligned}$$

where the structure factor S (2.14) arises from assuming spherically symmetric atomic potentials and pseudopotentials. From Sec. III, $\mathbf{\Lambda}$ is the operator

$$\mathbf{\Lambda}=(\hbar/4m^2c^2)\nabla V\times\mathbf{p}, \quad \text{(A4)}$$

but is approximated by

$$\mathbf{\Lambda}=\sum_{\text{all atoms } i}\xi(|\mathbf{r}-\mathbf{r}_i|)\mathbf{l}(\mathbf{r}-\mathbf{r}_i), \quad \text{(A5)}$$

when it is acting upon the core states $|b_t\rangle$. In the latter case, the plane waves and the core states are expressed in terms of spherical harmonics $Y_l{}^m$, so that

$$b_{nlm}(\mathbf{r})=R_{nl}(r)Y_l{}^m(\theta,\phi), \quad \text{(A6)}$$

and

$$e^{i\mathbf{k}\cdot\mathbf{r}}=\sum_{l=0}^{\infty}i^l[4\pi(2l+1)]^{1/2}j_l(kr)Y_{l\mathbf{k}}, \quad \text{(A7)}$$

where $\mathbf{Y}_{l\mathbf{k}}(\theta,\Phi)$ is the spherical harmonic with the rota-

[42] M. Miasek, Phys. Rev. **130**, 11 (1963).

[43] S. Golin is presently calculating the band structure of bismuth (private communication).

tional index $m=0$ in any coordinate system with z in the k direction.

The matrix element between plane waves is

$$\mathbf{\Lambda}^{PP}=\frac{h}{4mc^2}\frac{1}{\Omega N}\times\Big[\int_{\text{all atomic cells}} e^{-i\mathbf{k}'\cdot\mathbf{r}}\nabla V\times\mathbf{p}e^{i\mathbf{k}\cdot\mathbf{r}}d^3r\Big], \quad \text{(A8)}$$

where Ω is the volume of the atomic cell. Taking advantage of Eq. (3.4), the integral is

$$\int e^{-i\mathbf{k}'\cdot\mathbf{r}}\nabla V\times\hbar\mathbf{k}e^{i\mathbf{k}\cdot\mathbf{r}}d^3r$$
$$=-ih\int(\mathbf{k}-\mathbf{k}')\times\mathbf{k}Ve^{i(\mathbf{k}-\mathbf{k}')\cdot\mathbf{r}}d^3r$$
$$=ih\mathbf{k}'\times\mathbf{k}U(|\mathbf{k}'-\mathbf{k}|)S(\mathbf{k}-\mathbf{k}')\Omega N, \quad \text{(A9)}$$

where the Fourier transform of the potential has been expressed in the form (2.13).

All the integrals in $\mathbf{\Lambda}^{pc}$ and $\mathbf{\Lambda}^{cc}$ can be factored into their angular parts, and their radial parts. The radial integrals which depend on $\mathbf{k}$ are

$$A_{nl}(\mathbf{k})=\Omega^{-1/2}\int_0^\infty i^l(4\pi(2l+1))^{1/2}j_l(k'r)\xi(r)\times R_{nl}(r)r^2dr \quad \text{(A10)}$$

and

$$B_{nl}(\mathbf{k})=\Omega^{-1/2}\int_0^\infty i^l(4\pi(2l+1))^{1/2}\times j_l(kr)R_{nl}(r)r^2dr. \quad \text{(A11)}$$

The j_l are spherical Bessel functions. The B_l are the familiar orthogonality coefficients of the OPW method. For small k, both the A_l and the B_l are proportional to k^l,

$$A_{ln}\propto k^l,\ B_{ln}\propto k^l. \quad \text{(A12)}$$

This approximation is much better for A_{ln} than for B_{ln}, but even for B_l it holds extremely well. For example, for the outermost p and d core states, the most demanding relevant case, it holds within 1% in gray tin at values of the k vector twice as large as the Fermi k vector in white tin.

Now we need only compute the angular matrix elements

$$\langle Y_{l'\mathbf{k}'}|\mathbf{l}|Y_{l\mathbf{k}}\rangle=\langle Y_{l\mathbf{k}'}|\mathbf{l}|Y_{l\mathbf{k}}\rangle\delta_{ll'}. \quad \text{(A13)}$$

Throughout the derivation we use the notation of Condon and Shortley. Let the unit vectors in the k' and k directions be denoted by a and b, respectively, and let $|a\rangle$ and $|b\rangle$ denote the $Y_l^0(\theta,\Phi)$ quantized along these directions. Let $\{\hat{e}_1,\hat{e}_2,\hat{e}_3\}$ be a right-handed orthonormal basis, chosen so that

$$\mathbf{a}=\hat{e}_3,\quad \mathbf{b}=\hat{e}_1\sin\alpha+\hat{e}_3\cos\alpha. \quad \text{(A14)}$$

The problem is to compute the vector

$$\mathbf{M}=\langle a|\mathbf{L}|b\rangle. \quad \text{(A15)}$$

Since

$$\langle a|L_z=0, \quad \text{(A16)}$$

we need only compute M_x and M_y. The corresponding operators are

$$L_x=\tfrac{1}{2}(L^+ + L^-),$$
$$\text{and} \quad L_y=-\tfrac{1}{2}i(L^+-L^-), \quad \text{(A17)}$$

where the $L^\pm$ are the usual raising and lowering operators $L_x\pm iL_y$. From Eq. (A17) it is clear that only the $m=\pm1$ components of $|b\rangle$ contribute to M. This part of $|b\rangle$ will be called $|b'\rangle$. By the well-known addition theorem for the spherical harmonics,

$$|b'\rangle=(l(l+1))^{-1/2}P_l^1(\alpha)\{Y_l^{-1}-Y_l^1\}, \quad \text{(A18)}$$

where the functions P are the associated Legendre polynomials. By using the fact that

$$L^-Y_l^1=(l(l+1))^{1/2}Y_l^0,$$
$$\text{and} \quad L^+Y_l^{-1}=(l(l+1))^{1/2}Y_l^0, \quad \text{(A19)}$$

we arrive at

$$(L^+ + L^-)|b'\rangle=0, \quad \text{(A20)}$$

so that $M_x=0$. Also,

$$M_y=\langle a|L_y|b\rangle=-\tfrac{1}{2}i\langle a|(L^+-L^-)|b'\rangle$$
$$=-iP_l'(\cos\alpha)$$
$$=-i(\sin\alpha)(dP_l(\cos\alpha)/d\cos\alpha). \quad \text{(A21)}$$

Finally,

$$\langle a|\mathbf{L}|b\rangle=-i[dP_l(\cos\alpha)/d\cos\alpha)\mathbf{a}\times\mathbf{b}. \quad \text{(A22)}$$

The quantity in the brackets are 1 for $l=1$, and $\frac{3}{2}\cos\alpha$ for $l=2$. Naturally, this quantity is zero for $l=0$. These results allow the matrix elements of the spin part of the Hamiltonian to be written in their final, simple form:

$$\mathcal{H}_{\mathbf{k}'s',\mathbf{k}s}^{s-o}=-iS(\mathbf{k}-\mathbf{k}')[-(\hbar^2/4mc^2)U(|\mathbf{k}'-\mathbf{k}|)+\lambda_1+\lambda_2(\mathbf{k}'\cdot\mathbf{k})]\mathbf{k}'\times\mathbf{k}\cdot\boldsymbol{\sigma}_{s's} \quad \text{(A23)}$$

for a substance with only s, p, and d core states.